Organization of Self-Assembled Peptide−Polymer Nanofibers in Solution

Hans G. Börner,*,† Bernd M. Smarsly,†,° Jens Hentschel,† Anja Rank,‡ Rolf Schubert,‡ Yan Geng,§ Dennis E. Discher,|| Thomas Hellweg,⊥ and Astrid Brandt#

Max Planck Institute of Colloids and Interfaces, MPI KGF Golm, D-14424 Potsdam, Germany, Department of Pharmaceutical Technology and Biopharmacy, Albert-Ludwigs University, Stefan-Meier-Strasse 19, D-79104 Freiburg, Germany, Chemistry Department, University of Georgia, Athens, Georgia 30602, Chemical & Biomolecular Engineering, University of Pennsylvania, 112 Towne Building, Philadelphia, Pennsylvania 19104-6315, University of Bayreuth, Universitaetsstrasse 30, D-95447 Bayreuth, Germany, and Hahn-Meitner Institute, Glienicker Strasse 100, D-14109 Berlin, Germany

Received June 25, 2007; Revised Manuscript Received October 30, 2007

ABSTRACT: The solution structure and the aggregation behavior of stiff polymer−peptide nanofibers, self-assembled from well-defined poly(ethylene oxide)−peptide conjugates are described. Aqueous solutions at different concentrations of core−shell nanofibers were investigated by cryo-fixation transmission electron microscopy (*cryo*TEM) and small-angle neutron scattering (SANS). Both methods show the presence of stiff, extended nanofibers in dilute solution, providing nanodimensions for the fiber cross section, which are in good agreement with previously shown investigations on dried and deposited fibers. Moreover the previously suggested core−shell character of the fiber cross section could be verified by SANS density profiles. In concentrated solutions exceeding 2 mg/mL, the nanofibers tended to further organize into nematic "bundles". Polarized optical microscopy (POM) indeed shows birefringence of the solutions and typical Schlieren textures in shear oriented films, consistent with high aspect ratio nanofibers. The results of this investigation are discussed in the context of the Flory theory of rigid rods.

Introduction

Peptide−polymer conjugates represent an attractive class of macromolecules as they have the potential to combine self-organization properties with biological activity.[1−6] Short peptide segments in conjugates can in particular induce and guide molecular organization processes.[7−14] The peptide-guided organization of synthetic polymers exploits the inherent tendency of sequence defined polypeptides to adopt well-defined structures[15−17] and thus, enlarge the structural space, available for polymer aggregates in solution.[18,19] This biomimetic approach might also allow for dynamic and reversible structure formation due to soft and tunable interactions between the peptide segments. Potentially this leads to responsive or switchable structures as well as self-healing systems, which could be of interest for applications as functional elements in bioinspired materials sciences and synthetic biology.[18]

Formation of liquid-crystalline (LC) structures in solutions of rodlike objects or polymers was already observed by Flory as early as 1956,[20−22] showing that the process can be purely entropically driven. Nature exploits the formation of LC-domains to achieve materials with extraordinary mechanical properties related to the directional enforcement. Well-known examples include the self-organization of stiff biofibers such as collagen, actin filaments, microtubules, myosin filaments or cellulose fibers. The LC-structures lay the basis for the anisotropic stability of bones, the contractile function of muscles, the directed strength of the cytoskeleton or the rigidity of the plant body. Transferring this concept to synthetic, bioinspired materials is of great interest to achieve smartly reinforced, high performance materials of low density.[23−25]

Recently, we reported the synthesis and preliminary studies on self-organization properties of a well-defined conjugate (**I**), comprising a poly(ethylene oxide) block and an oligopeptide segment.[26] The latter consists of two pentapeptides (*dm*Gly-(Thr-Val)$_2$ that were attached to a template moiety, based on a derivative of carbazole. This template was designed to preorganize the short peptide strands into an appropriate geometry, thereby greatly enhancing the aggregation tendency to adopt the β-sheet secondary structure motif formation.[26−28] The careful deaggregation and controlled reaggregation of **I** in water results in the formation of nanotape structures.[26] Initial AFM and TEM analysis reveal the strongly anisometric dimensions of the cross section of the structures, exhibiting a width of 13−17 nm and a height of 1.4 nm, respectively. The maximum length was about 2 μm. Peptide strands adopt a well-defined β-sheet secondary structure as detected by CD−UV-spectroscopy (CD). On the basis of the observed β-sheet structure, the fiber dimensions and the aggregation behavior of congener model systems[28,29] an aggregation model was suggested.

As schematically outlined in Figure 1, the hierarchical assembly process of the conjugates is induced and guided by the self-organization of the peptide segments. These are forming a central tape structure by adopting an antiparallel β-sheet motif (Figure 1b). The resulting tapelike structure is highly stable and possesses a peptide core with a width of about 2.8 nm, as

* To whom correspondence should be addressed. E-Mail: hans.boerner@mpikg.mpg.de. Telephone: +49 (0)331-567-9552. Fax: +49 (0)331-567-9502.

† Max Planck Institute of Colloids and Interfaces, MPI KG Golm.

‡ Department of Pharmaceutical Technology and Biopharmacy, Albert-Ludwigs University.

§ Chemistry Department, University of Georgia.

|| Chemical & Biomolecular Engineering, University of Pennsylvania.

⊥ University of Bayreuth.

Hahn-Meitner Institute.

° Present address: University of Giessen, Institute of Physical Chemistry, Heinrich-Buff-Ring 58, D-35392 Giessen, Germany.

10.1021/ma0714060 CCC: $40.75
Published on Web 01/26/2008

Scheme 1. Chemical Structure of I (*dm*Gly, *N*,*N*-Dimethylglycine; Thr, Threonine; Val, Valine)

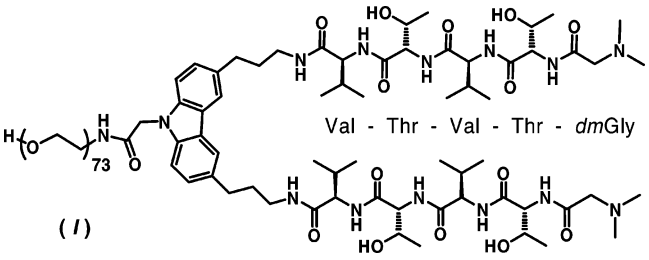

estimated from low level computer simulations, and a PEO-shell with twice 4.6 nm. The height of 1.4 nm of the observed structures cannot be explained by a single β-sheet (Figure 1b). Hence, the formation of a double tape by the distinct stacking of two β-sheets is most likely (Figure 1c). Such structural motif occurs rather frequently in biological systems with a stacking height of about 0.9−1.2 nm and is denoted as a "ribbon".[29] Formation and stabilization of the ribbons is probably driven by entropy via the hydrophobic effect. The aggregation of the $(Val\text{-}Thr)_2$-domains into antiparallel β-sheets leads to the formation of sheet structures with facial amphiphilicity. These associate via the hydrophobic faces resulting in the formation of a hydrophobic core (cf. Figure 1c, side view).

Nanotapes were observed by dry-state investigations of substrate deposited aggregates with atomic force microscopy (AFM) and transmission electron microscopy (TEM).[26] Here we extend the work to solution studies on such self-assembled nanotapes (in particular using small-angle neutron scattering), investigating both the fine structure of the nanotapes in solution and the hierarchical assembly of these, leading to LC-domains. To assess the aggregation and self-assembly behavior, a series of solutions were studied with different concentrations. The aggregation behavior is discussed in terms of the Flory theory of rigid structures.

Experimental Part

Materials and Methods. Materials and methods for the synthesis of I were reported previously.[26] Briefly, the conjugate **I** was synthesized using automated solid-phase supported peptide synthesis (SPPS). The TentaGel PAP resin (PEO attached polystyrene resin) was applied as solid support. This resin allows the stepwise assembly of the peptide segment directly at the resin-attached PEO block and thus, the complete PEO−peptide conjugate can be liberated from the support after SPPS. In the first step, the template molecule was attached to the PAP resin as an amino protected diamino acid derivative of carbazole (3,6-bis(3-[*N*-[*tert*-butoxycarbonyl]amino]propyl)carbazol-9-acetic acid). After quantitative coupling, the amino groups were deprotected and subsequently amino acids were attached, assembling two repeats of alternating valines and threonines followed by N-terminal capping with *N*,*N*-dimethylglycine (*dm*Gly). The $(dmGly\text{-}Thr\text{-}Val\text{-}Thr\text{-}Val\text{-}NH)_2$-template-$PEO_{72}$ conjugate (**I**) was cleaved from the resin, isolated in about 45% yield, and the successful synthesis could be confirmed by MALDI−TOF mass spectrometry.

Instrumentations. Circular dichroism UV spectra were recorded in solution on a Jasco 715 CD spectrometer using about 1 mg/mL sample concentration. Exact concentration was determined by UV spectroscopy via calibration against the 297 nm absorption of the carbazole derivative.

Transmission electron cryo-fixation microscopy (*cryo*TEM) was performed on a Zeiss EM LEO 912Ω instrument (Zeiss, Germany) at an acceleration voltage of 120 kV and "zero-loss" conditions. The samples were prepared as described in the supporting section. Atomic force microscopy (AFM) was performed on a NanoScope IIIa device (Veeco Instruments, Santa Barbara, CA) in tapping mode. The samples were spin-coated (4000 rpm) from solution (0.05−0.5 mg/mL) on freshly cleaved Mica substrates. Polarized optical microscopy (POM) was performed with a Leica DMR optical microscope.

Small-Angle neutron scattering (SANS) experiments were carried out at the Instrument V4 of the Hahn-Meitner-Institut (HMI) in Berlin (Germany), which is installed on the neutron guide NL 3A (cold source). The neutron wavelength was set to 6 Å, with a spread of ca. 10%. All measurements were performed at three sample-to-detector distances (1, 4, and 16 m) covering a q range from 0.003 $Å^{-1}$ up to 0.36 $Å^{-1}$. SANS was performed on solutions in deuterated water with concentrations of **I** of 110, 60, 30, 10, 6, and 1 mg/mL. The data were collected on a two-dimensional detector with 64 × 64 quadratic elements of the dimension 10 mm × 10 mm, the virtual resolution of the detector was set to 128 × 128 cells of 0.5 mm × 0.5 mm. The data were corrected for the efficiency of the different detector cells using water as reference sample and were circularly averaged afterward. After correction for the scattering of the solvent and the empty cell, the data were brought to absolute scale.[30] All the data reduction steps described above were performed using software provided by the HMI (BerSANS software package).[31,32]

Results and Discussion

The structural model given in Figure 1 was established in part on the bases of microscopy investigations of non-solvated structures deposited on solid substrates that include carbon-coated copper grids for TEM and mica for AFM measurements. Even if similar structures and conclusive structural dimensions could be observed despite the different surface energies of the substrates, an investigation of the solution structure is required to exclude surface-induced structure formation or reorganization processes.

Cryo-fixation TEM (*cryo*TEM) experiments were performed to provide insight into the self-assembled tape structures in "quasi solution". Figure 2 (left) shows an overview micrograph that shows the presence of extended structures with a positive contrast compared to the glassy water matrix. The observed aggregates exhibit polydisperse lengths, reaching a maximum of ∼1.5 μm and correspond well to these from the dry-state investigations.[26] Apparently the structures are relatively robust, because substrate deposition does not disrupt the nanotapes as has been described previously for other stiff molecules and molecular aggregates.[33] From the visible correlation between the orientations of neighboring fibers, there is a strong tendency to form bundles evident. The relatively low mean curvature of the filaments indicates a significant persistence length, which is consistent with the proposed model and can be explained by the rigidity of interactions as well as robustness of extended β-sheets. The conformational freedom of β-sheet structures is mainly restricted by the nature of the hydrogen bond that stabilizes the structure. Since the binding energy contribution of H-bonding is strongly sensitive toward torsion and distance only limited flexibility of the structures is tolerated.

Precise dimensions can be extracted from a *cryo*TEM micrograph with higher magnification (Figure 2 (right)). The peptide core of the fiberlike structures (Figure 1c) appears with a higher contrast compared to both the highly solvated PEO-shell and the glassy water matrix. An inner core diameter can therefore be determined to be 3.6 ± 0.6 nm. It should be noted that the error of this value is rather high, due to the low contrast of the structures for the electron beam. However, the value agrees fairly well with the diameter of 2.8 nm predicted by rudimentary computer simulations of $(dmGly\text{-}Thr\text{-}Val\text{-}Thr\text{-}Val\text{-}NH)_2$-template molecules in an antiparallel β-sheet arrangement, particularly considering that the PEO chains closest to the hydrophobic carbazole template are probably less solvated and more densely packed. Thus, these inner chain segments might contribute to the visible core structure, too.

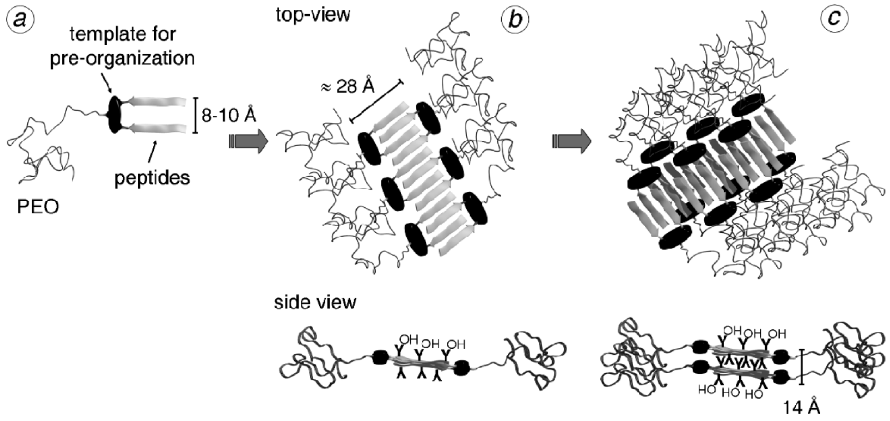

Figure 1. Schematic presentation of the organization of **I** (a) into fiberlike aggregates, showing a peptide β-sheet core and a PEO-shell (single β-sheet (b) and ribbon structure (c)). The numbers of threonine and valine side chains in the side views are reduced due for clarity.

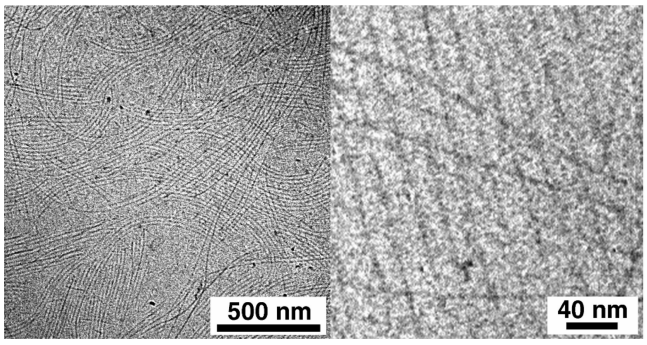

Figure 2. *Cryo*TEM micrographs of bundles of the anisometric aggregates of **I** in water (2 mg/mL).

It is important to note that artifact formation and the projection of the 3D structures into a 2D plane prevents to draw further conclusions concerning the spatial distribution and 3D packing of the nanofibers as well as of the bundles in bulk solution. During sample preparation for *cryo*TEM a drop of the sample solution is placed on a TEM grid. After blotting off the excess solvent a thin liquid film is obtained, adopting a meniscus-like shape in the holes of the grid. It is a well-described phenomenon that this can force nano-objects like, e.g., self-assembled wormlike micelles into the thicker regions of the film, leading to apparently higher packing density of the objects.[34,35] However, it was shown that this compression effect is rater weak and usually does not influence the dimensions of individual aggregates (e.g., nanotapes). Moreover, it can even be exploited to determine the dimensions of self-assembled structures because the forced close packing allows estimating dimensions of structure segments composed of, e.g., PEO, which possess a low contrast for the electron beam. In the present case, a homogeneous spacing between the visible core structures can be observed in close parallel packing of fibers (Figure 2 (right)). The relatively large average spacing of 20 ± 2 nm is due to the PEO shell, shielding the core and preventing lateral interactions of the peptide structures. Compared to the dry, non solvated structures, which show a width of about 13−17 nm, a volume increase of the hydrated PEO chains is expected and therefore consistent with the structure model. The *cryo*TEM results suggest lateral dimensions of the PEO-shell of about ∼16 nm (2×8 nm (PEO) + 4 nm (peptide core) $\approx$ 20 nm). Considering that the diameter of gyration of an undisturbed PEO-coil is ∼2.5 nm, it can be estimated that the PEO coils adapt a slightly stretched chain conformation (∼25% elongation). Coil deformation is, however, expected not to reach the brush regime (∼25 nm contour length of the PEO-chain), because the distance between neighboring PEO-chains is rather large (about 1 nm). This prevents strong sterical pressure as, e.g., present in macromolecular bottle brushes, where side chain spacing is frequently ∼0.24 nm.

Strong dilution of the aggregate solution from 2 mg/mL to 0.02 mg/mL separates the fibers even under *cryo*TEM sample preparation conditions (cf. Figure S1). A loss in molar ellipticity in the CD spectra due to dilution effects cannot be detected. This finding supports the proposed structure model, because lateral interactions of the fibers are regarded to be weak due to the PEO-shell, and thus fiber separation should occur upon dilution. Moreover, it indicates the extraordinary stability of the β-sheet secondary structure motif that stabilizes the fiberlike aggregates. This robustness is potentially important for the understanding of natural amyloid fibers, occurring, e.g., in neurodegenerative diseases including Alzheimer's disease.[36] These pathogenic fibrillar aggregates are insoluble and exceptionally stable, including resistance to enzymatic degradation.

Separated fibers could be evaluated by a fiber-segment correlation function (tangent-vector correlation).[37,38] On the basis of a rather limited statistical data set a rough estimation of the average persistence length is about $\lambda = 10 \pm 4$ μm, which approximates the persistence lengths of stiff biofibers such as actin filaments.[38−40]

The different microscopic analyses of the tape structures either deposited on a solid substrate or in quasi solution suggest a high tendency to form bundles, most likely due to the existence of extended LC-phases in the phase diagram. Therefore, a series of aqueous solutions with different concentrations, ranging from 110 mg/mL to 0.1 mg/mL (11−0.01 wt %) was investigated. As it could be expected, the increase in concentration leads to a viscosity increase of the solutions. However, the formation of a gel above the fluidic flow limit could not be observed in any case. Instead the trapping of air-bubbles in the solution with concentrations >5 mg/mL indicates probably the presence of rather fragile multipoint interactions between the fiber structures. Detailed rheological investigations are in progress and will be reported elsewhere. For solutions with concentrations >2 mg/mL (>0.2 wt %), birefringence was detected by polarized light microscopy, indicating the presence of ordered microdomains in solution. A more detailed structure of these LC-domains was accessed by the investigation of a thin film of a shear oriented solution with 24 mg/mL. Figure 3 shows the typical Schlieren texture, suggesting a hexagonal, nematic order.[41,42] The occurrence of liquid crystallinity with nematic order is consistent with the nature of the structures, if stiff fiberlike mesogens are considered that show a broad distribution in fiber lengths. However, in contrast to the predictions of Flory no macroscopic phase separation occurs, even after a year of sample storage,

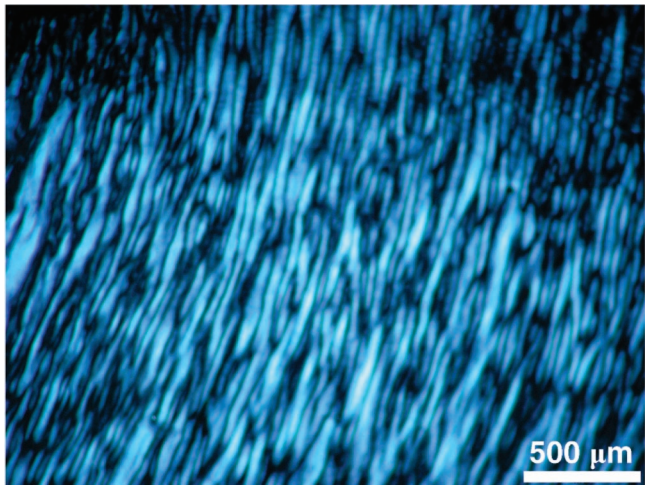

Figure 3. Polarized optical microscopy (crossed polarizers) of a thin film, shear oriented by wipe coating of an aqueous solution (24 mg/mL; shear direction from left to right).

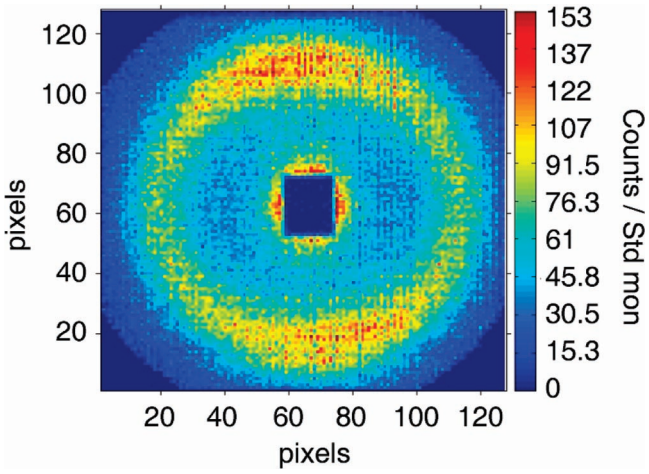

Figure 4. SANS pattern of the most concentrated solution (110 mg/mL), taken at a sample−detector distance of 8 m.

demonstrating that the obtained LC-domains are stable in solution.

It is accepted that imaging techniques might perturb self-assembled structures and even *cryo*TEM preparation artifacts might have an impact on the spatial distribution of the structures. Hence it is necessary to study the nanofibers in solution by means of scattering techniques, to investigate the bulk solution structure of the tapelike aggregates and the tape−tape interactions that lead to the formation of LC-domains. Small-angle neutron scattering (SANS) was performed on solutions in deuterated water with different concentrations between 110 and 1 mg/mL. Low concentrations (1 mg/mL) resulted in too weak scattering intensities and could therefore not be taken into account for further analysis. Interestingly, the solution at the highest concentration (110 mg/mL) produced an anisotropic SANS pattern (Figure 4). The scattering maximum resulting from the packing of the fibers is not isotropic, but indicates a preferred orientation of the fibers in the rather thin SANS cell. The shear that occurs during the filling of the cells is sufficient to induce orientation of the stiff, elongated structures. Such an observation is typical of LC structures and therefore in agreement with the LC-domain formation already described above. The SANS data were radially averaged for further quantitative analysis, thus assuming isotropic SANS patterns. The authors are aware that neglecting the anisotropy theoretically produces systematic errors in the SANS data evaluation analysis, but the anisotropy is weak and only observed for the highest concentrations. Furthermore, the separate analysis of small sections of the 2D SANS data was impeded by the moderate signal-to-noise ratio.

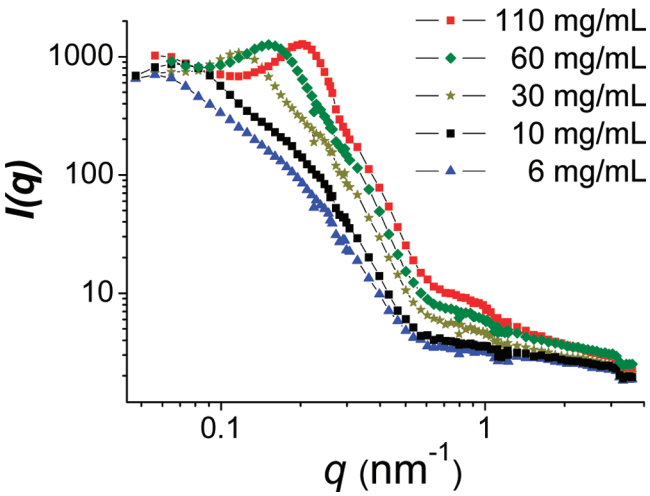

Figure 5. SANS data obtained from different solutions of the PEO−peptide nanofibers in D_2O at various concentrations.

The different radially averaged SANS curves are presented in Figure 5. Peculiar features are obvious, in particular a scattering maximum that shifts as a function of the concentration. Furthermore, all of the SANS curves exhibited a scattering minimum around $q = 0.6$ nm^{-1}, which can be interpreted as a minimum of a form factor. Hence, as a first conclusion the SANS curves correlate well with the packing of defined objects in the solution, and as could be expected, the average packing distance decreases upon increase in concentration.

In order to obtain quantitative information on the dimensions of the constituting objects and their mutual arrangement, different model functions were applied to analyze the SANS data by fitting, comprising appropriate parameters to account for disorder and object polydispersity. The considerable width of the scattering maxima and the rather broad minima can be taken into account by an analysis approach that has been recently introduced (cf. eq 1, where k is a scaling factor and I_B a constant background scattering).[43,44]

$$I(q) = k\,(\langle |F_{Cyl}(q)|^2 \rangle + |\langle F(q) \rangle_{Cyl}|^2 (S(q)_{Rosenfeld} - 1)) \times H_z^2(q) + I_B \quad (1)$$

In essence, the approach of Rosenfeld[45,46] is utilized to access the structure factor $S_{Rosenfeld}$, considering that the objects (fiberlike structures) possess a high aspect ratio, and therefore, their mutual arrangement can be described by a radially averaged 2D structure factor (describing the mutual arrangement). It is important to note that the Rosenfeld structure factor represents the "2D version" of the Percus−Yevick structure factor. The scattering of the nanofibers themselves is described by the form factor F_{Cyl} of infinitely long cylinders with a certain number distribution of the radius (polydispersity of the cross section), indicated by the $\langle\ \rangle$ brackets. The wavelength polydispersity of the V4 beamline (HWHM ca. 10%) was correctly taken into account by smearing of eq 1 with a Gaussian of the corresponding width. Subsequently our approach provides the following fitting parameters concerning the structure: (i) The first is the the average distance D between the nanofibers. (ii) Then there is the volume fraction ϕ within the concept of the Rosenfeld structure factor. Owing to the 2D nature of the Rosenfeld structure factor and the assumption of infinitely long cylinders,

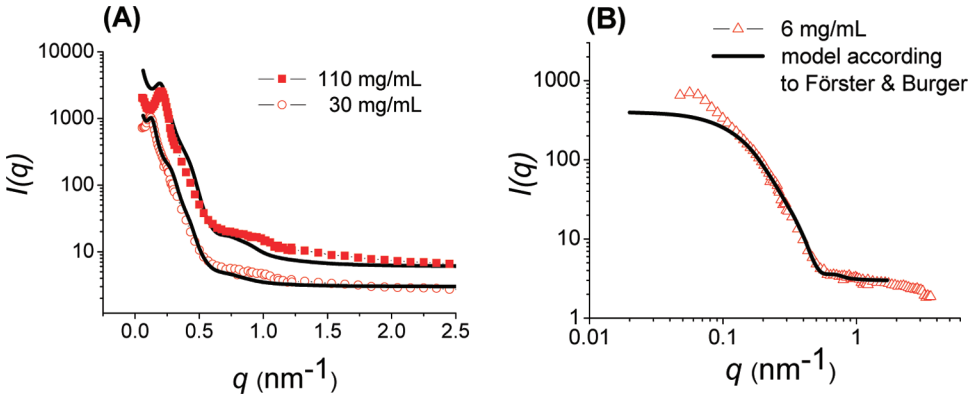

Figure 6. (a) Fittings of the SANS data, obtained from solutions of the PEO−peptide nanofibers with concentrations of 30 mg/mL and 110 mg/L and (b) fitting of the SANS data of a nanofiber solution with a concentration of 6 mg/mL applying the approach of Förster and Burger.[48]

ϕ thus is the ratio of the area occupied by the cylinder (fiber) cross section in relation to the total area (fiber diameter + water) occupied by the bundles. (iii) Finally there is the average radius R and its variance (form factor). Furthermore, a finite width d_z of the interface between fibers and water was taken into account, which is described by the function $H_z^2(q)$.[47] Figure 6a shows the analysis of two exemplary SANS data sets, obtained from solutions with concentrations of 110 and 30 mg/mL by applying the model described above. Although the SANS curves cannot be fitted in the sense of a perfect match between the experimental and theoretical curve, the shape and the main features of the experimental data are reasonably modeled, particularly the curve shape between the maximum and the minimum. It should be noted that the approach in eq 1 assumes a two-phase phase system regarding the scattering length densities. Within this model, the gradual transition in the scattering length densities between the fibers and D_2O is only described by the interfacial width d_z, but obviously such a simple approach is sufficient to account for the shape of the SANS curves. By evaluating all SANS curves, a rather constant average diameter of the cross section of 12−13 nm ±2 nm was obtained with $d_z = 2 \pm 0.5$ nm, which seems to be different from the core diameter obtained from TEM (3−4 nm). Nevertheless, it should be taken into account that these SANS experiments probed the scattering contrast between the solvent (D_2O) and the entire cross section of the objects, not just the inner peptide β-sheet core. A diameter of 12−13 nm, obtained for all the concentrations used in this study, is consistent with the cross section of the entire nanotapes, including the swollen PEO shell. The deviation between the diameter determined from *cryo*TEM micrographs and that based on the SANS analysis is, however, only apparent in nature. It can be explained by statistic rotation of the nanotapes along the tape main axis. Thus, in average a fiberlike object with an elliptical or even spherical cross section can be observed with SANS. It is straightforward to rationalize that the rotation of a flat tape with cross-sectional dimensions of approximately 20 × 2 nm (width × height) might appear as an object with spherical cross section of ∼11 nm. This model however is rather simple, because on the one hand the height of the nanotape was taken from dry state AFM measurements and on the other hand the scattering contrast along the cross-section was set constant and does not follow gradually the density profile.

It should be noted that the SANS curves are governed by the form factor of the fibers at lower concentrations. Under these conditions, the SANS data can be well fitted at larger q, neglecting the structure factor $S(q)$ by just using the form factor of polydisperse, infinitely long cylinders (cf. Figure 6b). Only at small q ($q < 0.15$ nm^{-1}) a deviation from the model, described by eq 1 is evident, in the vicinity of a weak scattering maximum.

In order to extract further details from the SANS data, the data set corresponding to the lowest nanofiber concentration (6 mg/mL) was analyzed with a recently developed approach.[48] Förster and Burger introduced a general concept for the calculation of scattering functions (i.e., form factors) of colloidal objects (micelles, vesicles, etc.) using analytical model functions, and particularly including polydisperse objects and core−shell structures. Assuming that the fibers are infinitely long and have a non-constant radial profile of scattering length density, the SANS curve taken for the low concentrations (e.g., $c = 6$ mg/mL) were fitted, using algebraic density profiles $\varphi(r) \sim r^{\alpha}$ (see Supporting Information). In this approach, the density profile consists of piecewise analytical functions $\varphi(r)$ in each of a number of concentric microdomains (here we chose three) of a compartmented particle, in this case the fiber. Thus, the fitting parameters were the radii, scattering length density and the exponents α_i of each microdomain i, and a background scattering I_B. In Figure 6b, it can be seen that the SANS curve was reasonably fitted, and only at small scattering vectors deviations are observed, which can be attributed to the weak interaction of the fibers. The data points at $q > 2$ nm^{-1} were not considered for the fitting, as this region of the SANS curves was mainly dictated by incoherent scattering from the solvent and thus did not contain information about the fibers. Interestingly, the fitting shows that the fibers exhibit a core of relatively high density with a radius of about 2 nm, which is in agreement with the SANS analysis described above (see the Supporting Information for the density profile), and a corona of significantly lower density with an algebraic density $\varphi(r) \sim r^{-0.9}$. The overall radius (including the corona) obtained from this analysis is ∼10 nm, which is in agreement with the other analyses. The presence of a quite drastic difference between the core and the corona density supports the validity of the SANS analysis based on eq 1, which was applied to the data sets of solutions with higher concentrations.

The exact dimensions of the monodisperse peptide core, however, could not be accessed via SANS measurements. This is probably due to the gradual decrease of the scattering length density of the PEO shell with respect to the solvent, making contrast match experiments with mixtures of D_2O and H_2O difficult. This interesting aspect is addressed by ongoing work, using fully deuterated PEO-blocks.

The detailed analysis of the SANS data also enables one to achieve insight into the aggregation behavior of the fiberlike aggregates. The application of the Rosenfeld approach outlined

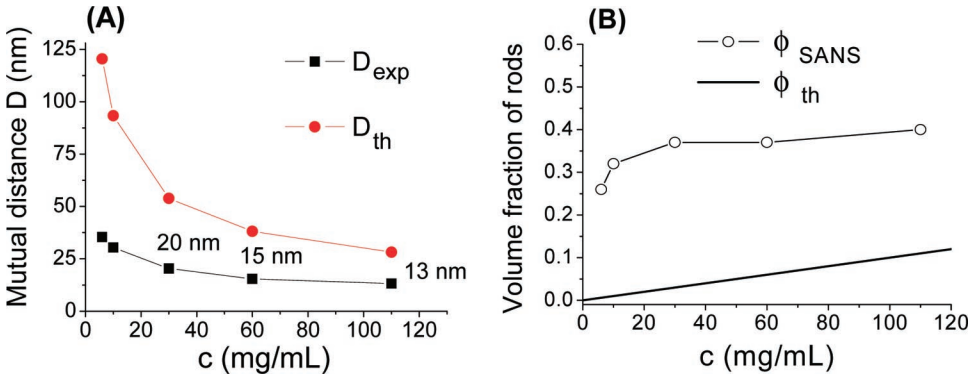

Figure 7. (a) Average distance between the fibers as determined from SANS (D_{exp}) and from eq 3 (D_{th}). (b) Comparison of the volume fraction of fibers within the aggregates (ϕ_{exp}) and the theoretical volume fraction based on eq 2 (ϕ_{th}).

in eq 1 provides the average mutual distance D and the volume fraction ϕ_{SANS} (defined as $V_{fiber}/(V_{fiber} + V_{water})$) as a function of the fiber concentration. It should be emphasized that the volume fraction ϕ_{SANS}, which was determined from the SANS model, represents the content of fibers within the aggregates, i.e., within bundles. Hence, in the case of aggregate formation (e.g., bundles), ϕ_{SANS} should differ from the volume fraction ϕ_{th} corresponding to the average solution concentration, which are connected to each other by eq 2, assuming a polymer density of 1 g/mL (the average solution concentration of the fibers was determined by UV spectroscopy, considering a homogeneous distribution of the fibers in solutions).

$$\phi_{th} = \frac{V_{polymer}}{V_{polymer} + V_{water}} = \frac{m_{polymer}}{m_{polymer} + m_{water}} \qquad (2)$$

Indeed, both D and ϕ_{SANS} show an interesting dependence on the concentration, when comparing the experimentally determined average distance D_{exp} obtained from scattering experiments with the theoretical distance D_{th} from the average concentration (cf. Figure 7a). In a simplistic approximation, D_{th} is calculated as the mutual distance of cylinders with radius R, placed onto a 2D hexagonal lattice, the space between them being filled by the solvent. For this calculation, R is taken from the SANS data analysis (see above) and ϕ_{th} was calculated by using eq 2. For a 2D hexagonal lattice, ϕ_{th}, R, and D_{th} are related to each other as expressed in eq 3

$$\phi_{th} = \frac{2\pi}{\sqrt{3}} \frac{R^2}{D_{th}^2} \qquad (3)$$

Thus, D_{th} can be calculated by using eqs 2 and 3. The absolute values of D_{th} have to be interpreted carefully due to the assumptions made. However, D_{exp} and D_{th} differ substantially and thus suggest the aggregation of the nanofibers. It is obvious that D_{exp} does not markedly change upon an increase in concentration. Moreover, the average distance of the fibers at higher concentrations could be determined with about 13 nm. This corresponds fairly well to the nanofiber diameter of 13.8 ± 1 nm as could be observed by AFM in close parallel packings of deposited fibers, making it likely that this value represents the maximum packing density of these fibers.

The formation of aggregates can be confirmed, additionally, if the volume fraction ϕ_{SANS} of the nanofibers as obtained from fitting of the SANS data is compared to the theoretical volume fraction ϕ_{th} that corresponds to a homogeneous distribution of the nanofibers (cf. Figure 7b). The local concentration of the nanofibers appears to be much larger, if compared to a homogeneous distribution of the nanofibers. This fact implies the presence of assemblies of nanofibers, e.g., into bundles. Furthermore, the experimental volume fraction appears to be rather resistant against dilution, highlighting the stability of the aggregates (e.g., bundles). The maximum packing density is already reached at low concentrations and further increase of the concentration, apparently only increases the domain size, diminishes edge effects and causing the pronounced peak in S(q).

Considering these observations, a simple packing model of stiff cylinders is applicable. Apparently the mesogens are stiff enough to exhibit an anisotropic regime in the phase diagram (e.g., formation of bundles). The most interesting result of the SANS experiments is the dependence of the bundle formation upon the concentration, suggesting the self-assembly of the fibers into a nematic mesostructure at already rather low concentrations. As indicated by the evolution of the packing density as a function of concentration, a transition between an isotropic solution and a self-assembled, nematic structure occurs at concentrations of ∼10 mg/mL (∼1 wt %). Such peculiar behavior can be explained by the Flory−Onsager theory, describing the solution behavior of rodlike structures.[20,21,49] One of the main predictions of this theoretical approach is the occurrence of a transition between isotropic and nematic LC structures at rather low concentrations and the occurrence of a small biphasic region.[21,50] These predictions are in full agreement with our experimental observations based on SANS.

The fact that the packing density is almost invariant upon compositional changes (cf. Figure 7b) suggests that the isotropic region of the phase diagram is below 10 mg/mL. This value is somehow unusually small, if, e.g., compared to polypeptide systems that adopt stiff α-helical structures, exhibiting transitions at about 100 mg/mL.[50] However, such behavior is constituent with the Flory−Onsager theory and can be explained by the large aspect ratio of the peptide−polymer nanofibers.[49,51] Simulations of the critical isotropic−LC transition volume fraction in terms of the Flory lattice model imply that for rigid rods the entropic costs of the LC-phase formation are markedly lowered with increasing structural anisotropy, thus driving the alignment of the rodlike structures into bundles. As an approximation, the theoretical limit of the volume fraction φ^* at which the anisotropic state may occur, is related to the aspect ratio P of the rods and can be described by eq 4.[52]

$$\varphi^* \approx \frac{8}{P}\left(1 - \frac{2}{P}\right) \qquad (4)$$

While polypeptides that adopt a stiff α-helical structure with, i.e., an aspect ratio of ∼100 exhibited a critical volume fraction φ^* of ∼8−10%,[50] the PEO−peptide nanofibers studied here have a critical volume faction φ^* of approximately 1−2%.

Estimating an aspect ratio of these nanofibers, roughly with 150 (2000 nm/13 nm) a critical volume fraction φ^* of ~5% should be expected, theoretically. The deviation between the experimental and theoretical values, might be interpreted that additionally to the entropic driving forces, which were predicted by Flory−Onsager theory to align stiff structure elements into bundles, also secondary interactions drive the bundle formation in solution. These could be, e.g., the entropically driven binding of PEO to the inherently hydrophobic β-sheet faces, via hydrophobic effects. Such interactions are well-described for other PEO−peptide conjugates and are discussed to cause an increased stability of, e.g., coiled-coil structures against thermal denaturation.[7]

Conclusion

In summary, the solution structure and the aggregation behavior of peptide−polymer nanofibers, self-assembled from poly(ethylene oxide)−peptide conjugates were investigated by cryo fixation transmission electron microscopy (*cryo*TEM) and small-angle neutron scattering (SANS). Both methods confirm the presence of rather stiff, extended nanofibers in dilute aqueous solutions and evidenced the high tendency of these fibers to pack into well-defined aggregates (i. e., the formation of "bundles") if the concentration was increased above 2 mg/mL. The latter was verified by polarized optical microscopy, showing birefringence of solutions with concentrations >2 mg/mL. Moreover, typical Schlieren textures could be observed in shear oriented films, suggesting the presence of lyotropic nematic mesophases.

Consistent with the given structure model of the PEO−peptide nanofibers, a core−shell structure of the individual fibers was observed by *cryo*TEM. The diameter of the visible peptide core was determined with ~3.6 nm and an overall structure diameter of ~20 nm suggests the presence of a PEO-shell of about 16 nm. These dimensions agree well with previously reported values from dry state atomic force microscopy (AFM) and transmission electron microscopy (TEM) investigations, if the swelling of the PEO-shell is taken into account.

The structural dimensions and the core−shell character of the PEO−peptide nanofibers were conclusively verified by SANS experiments on solutions with different concentrations (from 6 to 110 mg/mL). Solutions with higher concentrations were described with a model, assuming a form factor of infinitely long cylinders with circular cross-section. On the basis of this model, a rather constant average diameter of the cross section of 13 ± 2 nm was determined for all concentrations. Moreover a core−shell structure of the fiber cross section was confirmed by the application of the approach of Förster and Burger to fit a SANS data set, measured at low fiber concentration. In addition, the analysis of the SANS data provided the average mutual distance D of the PEO−peptide nanofibers and the volume fraction ϕ. Considering the packing of stiff fibers into bundles (e.g., into a nematic 2D hex mesostructure) a minimum of the packing distance was calculated, revealing densely packed fibers with a diameter of ~13 nm. The exact dimensions of the monodispers peptide core, however, could not be accessed via SANS measurements. However, this interesting aspect is addressed by ongoing work, using fully deuterated PEO-blocks.

The understanding of the aggregation behavior of stiff polymer−peptide nanofibers, particularly at comparatively low concentrations, might allow for the design of artificial, fiber reinforced composite materials. As is demonstrated in biological materials, the generation of anisotropic properties frequently relies on the formation of liquid crystalline mesophases. The formation of nematic bundles appears to be suitable for fiber reinforced materials, because layer formation is prevented. This might allow the generation of high performance biomimetic materials with topologically interlocked interfaces that could dissipate high amounts of energy before rupture.

Acknowledgment. This work was supported by the German Research Foundation (DFG) through the Emmy Noether-Program (BO 1762/2-2), the Max Planck Society, and the HMI BENSC 1187/2006. We are grateful to Markus Antonietti for helpful discussions and to Jessica Brandt, Doreen Eckhardt, and Erich C. for contributions to this project.

Supporting Information Available: Text giving methods used for the synthesis, the characterization and self-assembly of **I** and figures showing the *Cryo*TEM micrograph, CD spectrum and SANS data (including data analysis according to Förster and Burger) of assemblies in solution, and AFM images of the aggregates deposited on MICA substrate. This material is available free of charge via the Internet at http://pubs.acs.org.

References and Notes

(1) Klok, H.-A.; Schlaad, H. Peptide Hybrid Polymers. In *Advances in Polymer Science*; Springer: Berlin and Heidelberg, Germany, 2006; Vol. 202, p 160.
(2) Börner, H. G.; Schlaad, H. *Soft Matter* **2007**, *3*, 394.
(3) Klok, H.-A. *J. Polym. Sci., Part A: Polym. Chem.* **2005**, *43*, 1.
(4) Tirrell, M.; Kokkoli, E.; Biesalski, M. *Surf. Sci.* **2002**, *500*, 61.
(5) Lutolf, M. P.; Hubbell, J. A. *Nat. Biotechnol.* **2005**, *23*, 47.
(6) Ratner, B. D.; Bryant, S. J. *Annu. Rev. Biomed. Eng.* **2004**, *6*, 41.
(7) Vandermeulen, G. W. M.; Tziatzios, C.; Klok, H. A. *Macromolecules* **2003**, *36*, 4107.
(8) Smeenk, J. M.; Otten, M. B. J.; Thies, J.; Tirrell, D. A.; Stunnenberg, H. G.; van Hest, J. C. M. *Angew. Chem., Int. Ed.* **2005**, *44*, 1968.
(9) Hentschel, J.; Krause, E.; Borner, H. G. *J. Am. Chem. Soc.* **2006**, *128*, 7722.
(10) Rosler, A.; Klok, H. A.; Hamley, I. W.; Castelletto, V.; Mykhaylyk, O. O. *Biomacromolecules* **2003**, *4*, 859.
(11) Collier, J. H.; Messersmith, P. B. *Adv. Mater.* **2004**, *16*, 907.
(12) Hentschel, J.; Borner, H. G. *J. Am. Chem. Soc.* **2006**, *128*, 14142.
(13) Jahnke, E.; Lieberwirth, I.; Severin, N.; Rabe, J. P.; Frauenrath, H. *Angew. Chem., Int. Ed.* **2006**, *45*, 5383.
(14) Vandermeulen, G. W. M.; Klok, H.-A. *Macromol. Biosci.* **2004**, *4*, 383.
(15) Creighton, T. E. *Proteins: Structures and Molecular Properties*, 2nd ed.; W. H. Freeman: New York, 1993; p 512.
(16) Aggeli, A.; Boden, N.; Zhang, S.; Editors, *Self-Assembling Peptide Systems in Biology, Medicine and Engineering*; Kluwer Academic Publishers: Dordrecht, The Netherlands, Boston, MA, and London, 2001; p 364.
(17) Nesloney, C. L.; Kelly, J. W. *Bioorg. Med. Chem.* **1996**, *4*, 739.
(18) Whitesides, G. M. *Small* **2005**, *1*, 172.
(19) Börner, H. G. *Macromol. Chem. Phys.* **2007**, *208*, 124.
(20) Flory, P. J. *Proc. R. Soc. London, Ser. A* **1956**, *234*, 60.
(21) Flory, P. J. *Proc. R. Soc. London, Ser. A* **1956**, *234*, 73.
(22) Wee, E. L.; Miller, W. G. *J. Phys. Chem.* **1971**, *75*, 1446.
(23) Fratzl, P.; Gupta, H. S.; Paschalis, E. P.; Roschger, P. *J. Mater. Chem.* **2004**, *14*, 2115.
(24) Gordon, J. E.; Jeronimidis, G.; Richardson, M. O. W. *Philos. Trans. R. Soc. London, Ser. A* **1980**, *294*, 545.
(25) Fratzl, P. *Curr. Opin. Colloid Interface Sci.* **2003**, *8*, 32.
(26) Eckhardt, D.; Groenewolt, M.; Krause, E.; Börner, H. G. *Chem. Commun.* **2005**, 2814.
(27) Schneider, J. P.; Kelly, J. W. *Chem. Rev.* **1995**, *95*, 2169.
(28) Lashuel, H. A.; LaBrenz, S. R.; Woo, L.; Serpell, L. C.; Kelly, J. W. *J. Am. Chem. Soc.* **2000**, *122*, 5262.
(29) Aggeli, A.; Nyrkova, I. A.; Bell, M.; Harding, R.; Carrick, L.; McLeish, T. C. B.; Semenov, A. N.; Boden, N. *Proc. Natl. Acad. Sci. U.S.A.* **2001**, *98*, 11857.
(30) Nordskog, A.; Futterer, T.; von Berlepsch, H.; Bottcher, C.; Heinemann, A.; Schlaad, H.; Hellweg, T. *Phys. Chem. Chem. Phys.* **2004**, *6*, 3123.
(31) Keiderling, U. *Appl. Phys. A: Mater. Sci. Process.—Mater. Sci., Proc.* **2002**, *74*, *Part 2*, Suppl. S1455.
(32) Keiderling, U. *Physica B* **1997**, *234*, 1111.

(33) Sheiko, S. S.; Sun, F. C.; Randall, A.; Shirvanyants, D.; Rubinstein, M.; Lee, H.; Matyjaszewski, K. *Nature (London)* **2006**, *440*, 191.
(34) Zheng, Y.; Won, Y. Y.; Bates, F. S.; Davis, H. T.; Scriven, L. E.; Talmon, Y. *J. Phys. Chem. B* **1999**, *103*, 10331.
(35) Nordskog, A.; Egger, H.; Findenegg, G. H.; Hellweg, T.; Schlaad, H.; von Berlepsch, H.; Bottcher, C. *Phys. Rev. E* **2003**, *68*.
(36) Walsh, D. M.; Lomakin, A.; Benedek, G. B.; Condron, M. M.; Teplow, D. B. *J. Biol. Chem.* **1997**, *272*, 22364.
(37) Geng, Y.; Ahmed, F.; Bhasin, N.; Discher, D. E. *J. Phys. Chem. B* **2005**, *109*, 3772.
(38) Ott, A.; Magnasco, M.; Simon, A.; Libchaber, A. *Phys. Rev. E* **1993**, *48*, R1642.
(39) Yanagida, T.; Nakase, M.; Nishiyama, K.; Oosawa, F. *Nature (London)* **1984**, *307*, 58.
(40) Riveline, D.; Wiggins, C. H.; Goldstein, R. E.; Ott, A. *Phys. Rev. E* **1997**, *56*, R1330.
(41) Chandrasekhar, S. *Liquid-Crystals*, 2nd ed.; Cambridge University Press: Cambridge, U.K., 1994.
(42) Demus, D.; Goodby, J.; Gray, G. W.; Spiess, H. W.; Vill, V. *Handbook of Liquid Crystals, Volume 3: High Molecular Weight Liquid Crystals*; 1998; p 532.
(43) Smarsly, B.; Goltner, C.; Antonietti, M.; Ruland, W.; Hoinkis, E. *J. Phys. Chem. B* **2001**, *105*, 831.
(44) Smarsly, B.; Thommes, M.; Ravikovitch, P. I.; Neimark, A. V. *Adsorpt.—J. Int. Adsorpt. Soc.* **2005**, *11*, 653.
(45) Rosenfeld, Y. *J. Chem. Phys.* **1987**, *87*, 4865.
(46) Rosenfeld, Y. *Phys. Rev. A* **1990**, *42*, 5978.
(47) Ruland, W. *J. Appl. Cryst.* **1971**, *4*, 70.
(48) Förster, S.; Burger, C. *Macromolecules* **1998**, *31*, 879.
(49) Onsager, L. *Ann. N.Y. Acad. Sci.* **1949**, *51*, 627.
(50) Miller, W. G.; Wu, C. C.; Wee, E. L.; Santee, G. L.; Rai, J. H.; Goebel, K. G. *Pure Appl. Chem.* **1974**, *38*, 37.
(51) Flory, P. J.; Leonard, W. J. *J. Am. Chem. Soc.* **1965**, *87*, 2102.
(52) Papkov, S. P. *Fibre Chem.* **1973**, *5*, 6.

MA0714060